

Fine-Tuning the Acid–Base Properties of Boron-Doped Magnesium Oxide Catalyst for the Selective Aldol Condensation

Tu N. Pham,^[a] Lu Zhang,^[a] Dachuan Shi,^[a] Mallik R. Komarneni,^[a] Maria P. Ruiz,^[b] Daniel E. Resasco,^{*[a]} and Jimmy Faria^{*[b]}

Controlled incorporation of dopants into the structure of metal oxide catalysts can be used to fine-tune their topological, chemical, and electronic properties. Conventional preparation methods (coprecipitation and impregnation) tend to produce materials with a limited extent of chemical interaction between metal oxide and dopant, small pore volume, and disconnected pore structure. Herein, we describe a combustion method to optimize both the porous structure of metal oxides and the chemical interaction with dopants. By exploiting the differences in melting points between metal oxide (MgO) and dopant (B), it is possible to create hierarchical mixed oxides with tail-

ored chemical structure. As a model reaction, we employed the aldol condensation of acetaldehyde to crotyl alcohol, a key intermediate step in the conversion of bioethanol to 1,3-butadiene, to show the unique characteristics of these materials. The B–Mg mixed oxide prepared by combustion exhibits an order of magnitude higher productivity of C4 products than conventional MgO and B–MgO. We anticipate that our approach could be extended to the development of other dual oxides with open structure for unrestricted diffusion and enhanced chemical interaction of acid and basic metal oxides.

Introduction

Metal oxides with strong basic character (e.g., MgO, BaO, and CaO) are often employed as catalysts in the aldol condensation of aldehydes and ketones to the corresponding unsaturated aldehydes and ketones. However, these catalysts typically result in poor selectivity and stability because of over-condensation that leads to coke deposition and rapid deactivation of the strong basic sites by adsorption of H₂O or CO₂.^[1,2] The addition of small quantities of acidic oxides (e.g., TiO₂, Al₂O₃, B₂O₃) can be used to adjust the basicity of the catalyst by reducing the strength of basic sites and providing acid sites.^[3–7] In previous studies, this doping has been typically accomplished by either coprecipitation of the two metal precursors or impregnation of the basic oxide with a solution of an acidic oxide precursor, followed by thermal treatment.^[6–12] However, these processes may lead to the formation of mixed oxides with low surface area, limited pore connectivity, and phase segregation.

To overcome these limitations, we have developed a method that exploits the differences in the mobility of magnesium oxide (MgO) and boron oxide (B₂O₃) during the combustion of citric acid at high temperatures. The large difference in melting points and the rapid formation of combustion fumes results in a high-surface-area metal oxide foam with hierarchical meso- and macroporous structure, in which the light B atoms become effectively stabilized in two distinct surfaces, one consisting in small MgO clusters enriched with trigonal coordinated boron species (BO₃) and the other consisting of flat surfaces containing tetrahedral boron species (BO₄). These catalysts have been tested for the selective aldol condensation of acetaldehyde to crotonaldehyde (CAL), crotyl alcohol (COH), and 3-butenol (3BOH), which are precursors for industrially important chemicals such as 1,3-butadiene, 1,4-butanediol, and 1-butanol, widely used in the polymer industry.^[13–15] Aldol condensation is a ubiquitous reaction in the organic chemistry toolbox, which has been widely applied in the production of functional molecules generally used as starting materials in the manufacturing of pharmaceuticals, solvents, polymers, and more recently, renewable fuels. This C–C bond forming reaction is relevant in the conversion of small oxygenates, typically obtained from biomass, into larger molecules of higher value.^[16]

[a] Dr. T. N. Pham, Dr. L. Zhang, Dr. D. Shi, Dr. M. R. Komarneni,
Prof. D. E. Resasco
School of Chemical, Biological and Materials Engineering
University of Oklahoma
Norman, OK, 73019 (USA)
E-mail: resasco@ou.edu

[b] Dr. M. P. Ruiz, Dr. J. Faria
Abengoa Research
C/Energía Solar 1
Seville, 41014 (Spain)
E-mail: ing.jimmyfaria@gmail.com

Supporting information and the ORCID identification number(s) for the author(s) of this article can be found under <http://dx.doi.org/10.1002/cctc.201600953>.

Results and Discussion

Synthesis of hierarchical boron-doped magnesium oxide

MgO is a well-known basic oxide with high ionic character and a rock salt crystal structure of tunable morphology and surface structure.^[17–19] MgO is well suited for applications in catalysis because it is possible to modify its acid–base properties for the control of reactivity as well as its porous structure to adjust the rates of mass transport and stability during reaction.^[3,20,21] In this work, we have used a combustion process to prepare a set of MgO catalysts with boron concentrations varying from 0 to 15 wt.%. At the high temperatures generated by the combustion process, boron oxide is expected to be highly mobile (melting point 450 °C), enabling the formation of a glassy B₂O₃–metal-oxide interface. This structure is expected to reduce the interfacial tension of the vapor–glass interface facilitating the stabilization of large voids. To characterize these unique materials, we have used a scanning electron microscope with focused ion beam (FIB–SEM) to generate a thin cross section of one of the samples containing 7.5 wt.% B–MgO (Figure 1). The sample was thin enough to allow us to

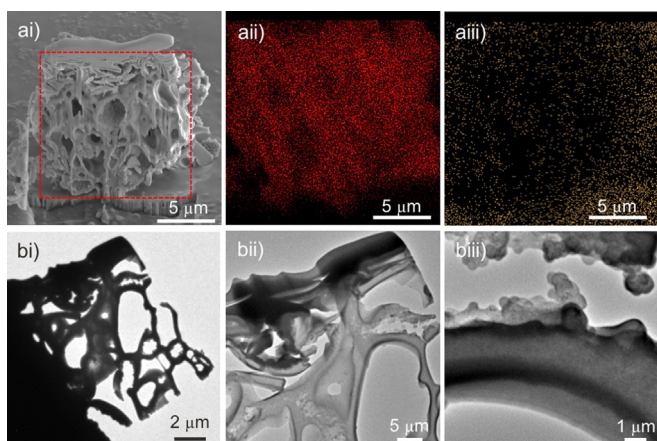


Figure 1. Cross-sectional characterization of the internal structure of B–MgO. ai) SEM analysis of the sample during FIB etching. ai,aii) EDX mapping of the cross section marked as a red square in (ai) demonstrating the microscopic distribution of Mg (red, aii) and boron (yellow, aiii). bi–biii) TEM analysis of the cross-section at three different magnifications.

image the internal structure by high-resolution transmission electron microscopy (HRTEM) along with energy-dispersive X-ray analysis (EDX). As shown in Figure 1ai–aiii, this material contains large void spaces that resemble those in a solid foam. Evidently, during the high-temperature synthesis, large bubbles of H₂O vapor and CO₂ were formed upon the rapid combustion of citric acid. These large cavities are interconnected by mesoporous channels created during the evacuation of the combustion gasses out the oxide and possibly affected the stabilization effect of B. As shown in Figure 1bi–biii, the surface of these chambers is covered by large clusters of Mg-enriched B–MgO and a smooth surface composed of glassy B₂O₃–MgO.

Mapping by EDX (Figure 1aii, aiii) corroborated that B and Mg were homogeneously distributed on the microscopic scale. Similar observations have been reported in TiO₂ thin films doped with small quantities of B, for which changes in surface free energy caused the creation of pores through grain-boundary grooves emerging from the bulk.^[4]

The pore-size distribution obtained with Barrett–Joyner–Halenda (BJH) analysis of N₂–desorption isotherms revealed that the MgO produced by the combustion method has a micro- and mesoporous structure (see Figure 2), but the addition of B

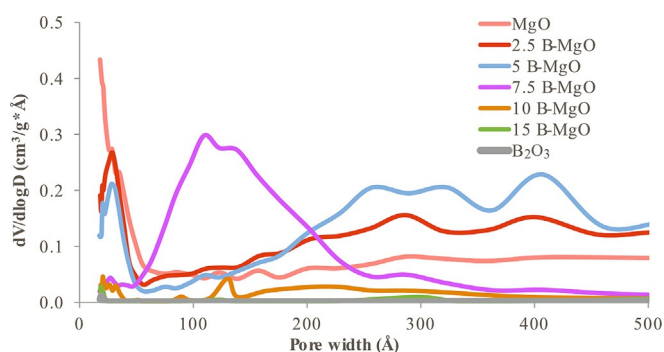


Figure 2. Pore-size distribution obtained from the BJH analysis of N₂ desorption isotherms of MgO, B₂O₃, and mixed B–MgO prepared by the combustion method with B content varying from 2.5–15.0 wt. %.

reduces the fraction of microporous and increases the meso- and macroporosity generating a hierarchical network. In the 7.5 wt.% B–MgO sample the pore-size distribution is rather uniform and centered at approximately 13 nm. In addition, there is a range of macroscopic pores observed by SEM that cannot be captured by the BJH analysis, which is valid within the 1.8–260 nm range. This is consistent with the formation of a hierarchical meso- and macroporous B–Mg structure. Clearly, the addition of B helps in the formation of a hierarchical structure and, as shown below, improves the basic–acid character of the material. However, excessively high concentrations of B have a detrimental effect on surface area. The specific surface area, determined by BET method progressively decreased from 223.5 m²g^{−1} to 6.7 m²g^{−1} as the B-content increased from 2.5 to 15.0 wt. % (see Table S2).

XRD profiles of the different B–MgO catalysts after calcination for 1 h at 500 °C are summarized in Figure 3. Five diffraction peaks are clearly apparent at diffraction angles of 37, 43, 62, 74, and 78°, which correspond to the (111), (200), (220), (311), and (222) planes of periclase MgO.^[22] The pure B₂O₃ sample prepared by the same combustion method, but without Mg showed an intense peak at 28.45°, which can be ascribed to the (311) plane of cubic B₂O₃.^[23,24] Remarkably, none of the mixed B–MgO oxides showed a noticeable diffraction intensity in any of the angles corresponding to B₂O₃ or Mg₃(BO₃)₂. Not a single additional diffraction peak was observed, which indicates that neither phase segregation of any of the two oxides nor formation of magnesium borates has taken place in any of the samples, even at the highest boron loadings (15 wt. %). Notably, as the B concentration increased,

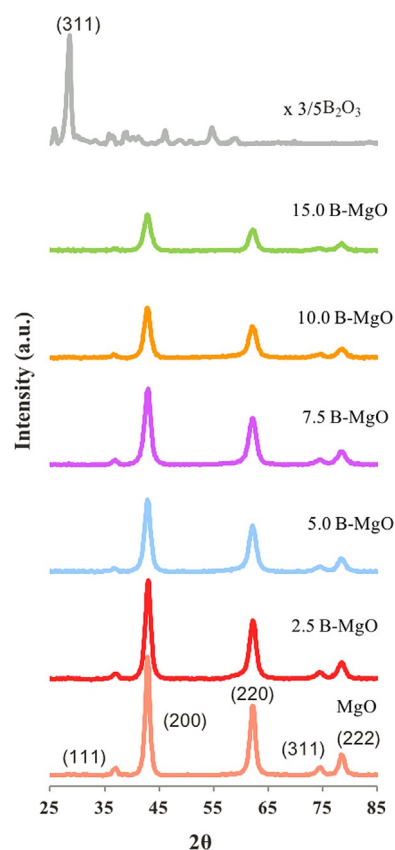


Figure 3. X-ray diffractograms of MgO, B₂O₃, and mixed B–MgO catalysts.

the peak area ratio of planes (200):(111) increased (Figure 4a), whereas the ratio of (200):(220) remained constant. The (111) surface is composed of alternating monolayers of highly polarized oxygen ions and magnesium cations (Figure 4b). This confers a strong electrostatic field perpendicular to the surface.^[25] This surface can be stabilized by the dissociative adsorption of water, in which a metal-terminated surface can become stabilized by OH groups while H protons are adsorbed on oxygen anions.^[26,27] By contrast, upon addition B, the (111) surface becomes less favored, whereas nonpolar planes, such as the (200) and (220) do not change. It has been shown^[28,29] that on rock salt structures the replacement of three M₁²⁺ cations by two M₂³⁺ in M₁O creates one M₁ vacancy that may act as a thermodynamic sink, which optimizes the lattice energy of the (111) surface. However, our observations indicate that this may not be the case in these B–MgO samples prepared by the combustion method described herein. A plausible explanation for our observations could be the reduction of electrostatic interaction between Mg and O layers if interstitial B³⁺ cations are present, thus limiting the rate of alternating ABABA growth.^[30,31] This kinetic effect might overcome the thermodynamically more favorable structure caused by the addition of M₂³⁺ cations. It seems that the resulting thermodynamically metastable state occurring during the synthesis of these B-doped MgO samples by the combustion process is favored by the high mobility of the low-melting-point B species, which allows a quick diffusion inside the MgO. Further confirmation

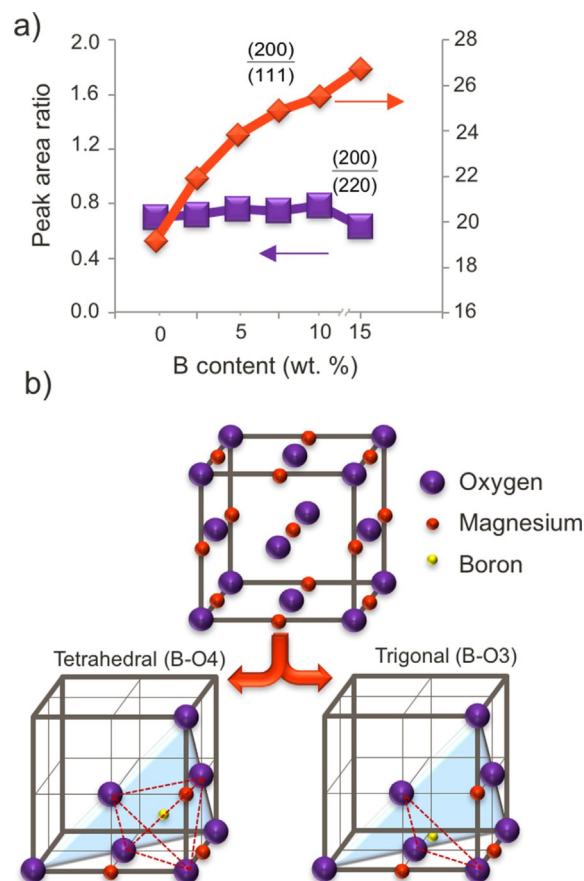


Figure 4. a) Effect of boron loading on the XRD intensity of different MgO planes. b) Schematic illustration of the (111) plane in MgO periclase crystal with B in MgO in trigonal and tetrahedral coordination.

of this was obtained by treating the sample containing 7.5 wt. % B–MgO in air at 1000 °C, much higher than those temperatures used above. XRD characterization of this overheated sample (Figure S6) revealed the formation of a separate crystalline structure corresponding to Mg₃(BO₃)₂ together with periclase MgO. The formation of highly crystalline magnesium borate phase and magnesium oxide can be attributed to the minimization of the free energy of the system.

The B³⁺ cation can occupy interstitial positions inside the MgO periclase structure in either trigonal or tetrahedral coordination (see Figure 4b). The different samples in the B-doped MgO catalyst series were further characterized by ¹¹B magic angle spinning (MAS) NMR spectroscopy (Figure 5), which provided crucial information to elucidate the coordination of B atoms in the MgO structure. For instance, in pure B₂O₃ boron has a trigonal configuration, triply coordinated to oxygen.^[32] In contrast, in all B-doped MgO samples, a mixture of trigonal and tetragonal ¹¹B signals was observed. By fitting these data using the method of Feng et al.^[33] (Table S4) it was possible to quantify the coordination sites of B. That is, for pure B₂O₃ two ¹¹B peaks with δ_{iso} chemical shift of 16.5 (B1) and 12 (B2) ppm were identified. They can be ascribed to trigonal B species in a boroxol ring (84.7%) and a BO_{3/2} network polymer (15.3%), respectively. Interestingly, on the 2.5 wt. % B-MgO sample pre-

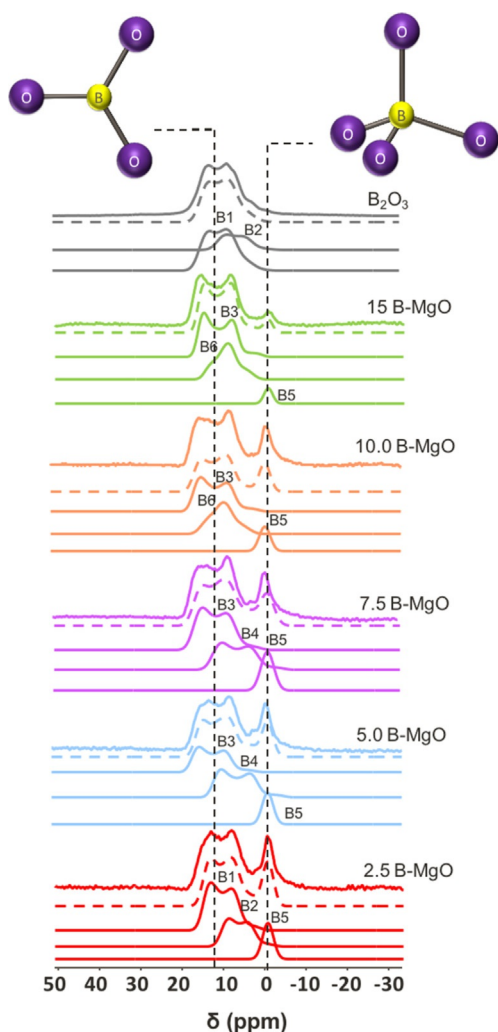


Figure 5. ^{11}B MAS NMR spectra of B_2O_3 and mixed B–MgO catalysts of different B contents. The top line gives the experimental spectrum and the lines below give the simulated spectra based on the work of Feng et al.^[33]

pared by combustion, in addition to the two B sites observed for pure B_2O_3 , a new B5 site was observed. This site corresponds to interstitial tetrahedrally coordinated boron (Q boron). Similar signals were observed on a 2.0 wt. % B–MgO sample synthesized by incipient wetness impregnation (IWI). However, the sample prepared by the combustion method showed a higher contribution of Q boron than that prepared by IWI, with abundances of 23% and 13.5%, respectively. The 7.5 wt.% B-doped MgO also showed three different B sites, but slightly different from those in the 2.5 wt.% B sample. In addition to the Q boron appearing at -1 ppm, those assigned to T boron and $\text{BO}_{3/2}$ polymer had a δ_{iso} chemical shift of 18.5 and 14 ppm. Although the simulated peaks for these sites (3 and 4) look very similar to those of sites 1 and 2 in pure B_2O_3 , they have different chemical shifts, which suggests that they have a different chemical environment. At even higher B concentrations (i.e., 15 wt. %) a new B site (B6) was observed with a δ_{iso} chemical shift of 15 ppm, which could be ascribed to a surface $\text{BO}_{3/2}$ polymer. The abundance of this species is about 14.9%, and interstitial T (B3) boron and Q (B5) sites amount to 78.5%

and 6.6%, respectively. This would indicate that, as the concentration of B increases trigonal $\text{BO}_{2/3}$ surface polymeric species begin to form. The lack of any B_2O_3 diffraction peaks along with the ^{11}B NMR data would indicate that these polymeric species are an amorphous glassy boron oxide that accumulates on top of the B-doped MgO.

The simultaneous coordination of B at interstitial positions and on the external surface has a remarkable effect on the electronic properties of the B–MgO, as shown by XPS data (Supporting Information, Figure S1). Upon addition of B, the first change that can be observed is a shift of the peak corresponding to Mg2p to higher binding energies. This systematic shift clearly increases with the B content, from 48.61 to 49.66 eV, and indicates that the presence of B^{3+} cations in MgO delocalizes the electronic cloud around the Mg^{2+} cations making them more electron deficient. Similar observations have been reported on Mg- and Cu-supported on metallic surfaces, in which chemical shifts to higher binding energies have been attributed to a combination of changes in the coordination number of the Mg atoms and charge transfer to the substrate.^[34,35] In parallel, the O 1s peak shifts to higher binding energies upon addition of B^{3+} . This shift has a crucial influence on the catalytic activity because, as the O^{2-} becomes less electron rich, its Lewis basicity decreases. To corroborate this trend in acid–base character, temperature-programmed desorption (TPD) was conducted with CO_2 (a probe of basic sites) and pyridine (a probe of acid sites). The results are summarized in Figures S2 and S3, respectively.

Electron microscopy images of the B–MgO materials are shown in Figure 6. All the B–MgO samples have a very similar surface topology (Figure 6a–i–e–i), consisting of thin platelets approximately 100 nm thick agglomerated in larger particles. Interestingly, the surface of these platelets is decorated with randomly distributed large clusters (80–100 nm, Figure 6c–i). Notably, this unique architecture is not observed either on MgO or B_2O_3 pure samples, prepared by the same combustion method. The pure MgO sample exhibited whiskers and needle-like structures, and the pure B_2O_3 sample displayed a flat topology without any special feature. Similarly nanostructured MgO materials have been previously obtained by employing polyol-mediated thermolysis, which favors the formation of highly reactive (111) MgO surfaces with increased basicity.^[36,37] However, the unique structure of the B-doped MgO reported here has not been previously observed.

More detailed characterization of this B–MgO structure was achieved by TEM bright-field (BF) and dark-field (DF) imaging (Figure 6a–ii–e–ii and a–iii–e–iii, respectively). In TEM–BF micrographs flat platelets with large aggregates are observed that protrude from the surface; similar to those observed by SEM. In TEM–DF a significant number of highly crystalline patches were observed on the different B–MgO as verified by the appearance of bright spots. These crystalline domains were significantly smaller than the larger aggregates observed by SEM and TEM–BF with sizes ranging from 5 to 10 nm. These crystalline patches were observed on both flat surfaces and larger clusters. Notably, the structure of these crystalline domains changed as the content of B increased (Figure 6a–iv–e–iv). At

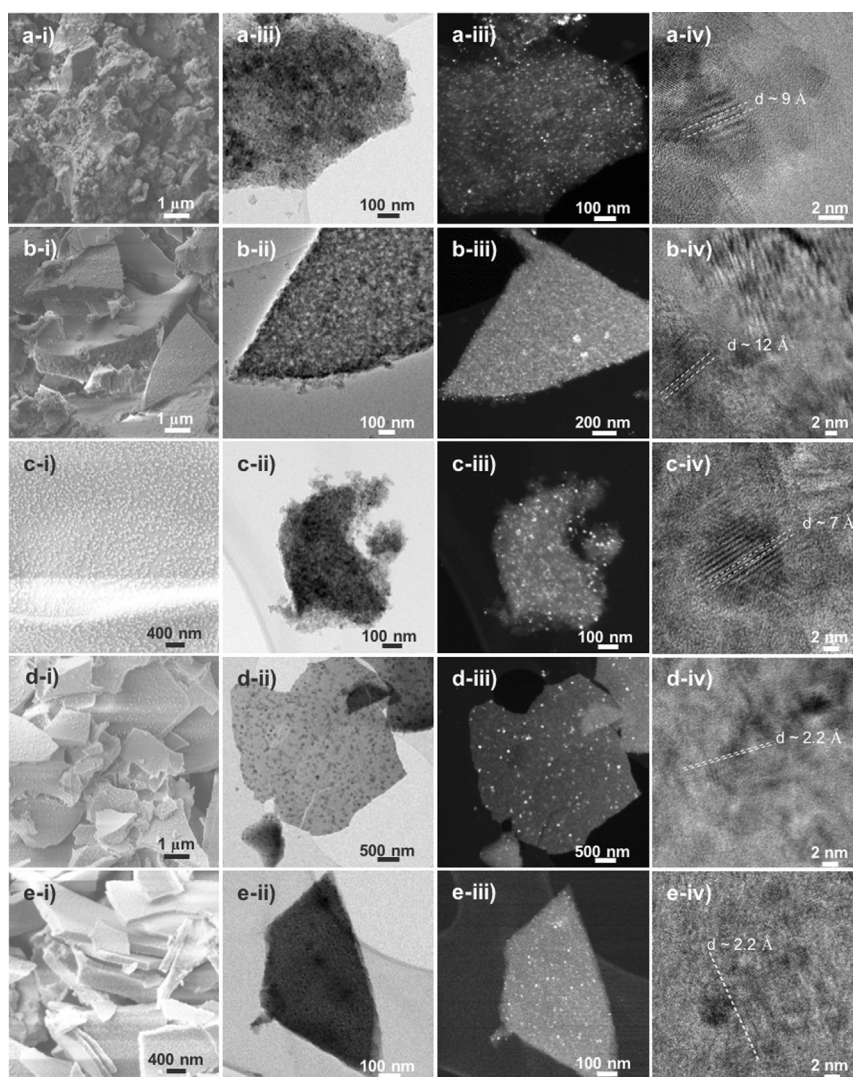


Figure 6. Complex nanoarchitecture of B-MgO catalysts. Topological and nanostructural characterization by (i) SEM, (ii) TEM bright field (BF), (iii) high-resolution (HR) TEM dark field (DF), and (iv) HRTEM-BF of the different catalysts, including MgO doped with a) 2.5, b) 5.0, c) 7.5, d) 10.0, and e) 15.0 wt.% B, respectively.

low B loadings (e.g., 2.5–5.0 wt.% B-MgO) the crystalline patches exhibited a combination of lattice fringes of large ($\approx 9 \text{ \AA}$) and small ($\approx 2.2 \text{ \AA}$) d-spacing. The large d-spacing can be attributed to mismatch lattices between two crystalline planes (Figure S5).^[38] The rotation angle of the two planes can be approximated by the ratio of the $d_{(200)}$ spacing (2.2 \AA) and large d-spacing obtained by HRTEM, which is a reasonable approximation because the rotation angle was below 30° ($\pi/6$). The resulting rotation angles of the sections shown in Figure 6a-iv–e-iv were 14 , 10.5 , and 18.2° for the 2.5, 5.0, and 7.5 wt.% B-MgO samples, respectively. Interestingly, at higher B concentrations, the lattice mismatch disappeared and lattice fringes in the (200) direction were predominantly observed.

The results obtained from the high-angle annular dark-field scanning transmission electron microscopy (HAADF-STEM) tomography of the mixed oxide containing Mg and B, with a B content of 7.5 wt.%, prepared by the combustion method, are shown in Figure 7. This imaging technique employs a set of 75

HAADF-STEM images of the mixed oxide particle taken every 2° from 75° to -75° of incidence angle. After careful alignment of the images using imageJ software the stack of images was employed to generate a computational 3D reconstruction of the morphology and topology of the mixed oxide on the nanometric scale. These results confirm that the large clusters are located on top of the flat surfaces and are crystalline, as confirmed by the electron diffraction from the clusters (Figure 7a-ii–a-iii). In addition, electron energy loss spectroscopy (EELS) was used to chemically characterize the materials. Figure 7b-i, b-ii shows the area mapped by aberration-corrected (AC) STEM-EELS of the 7.5 wt.% B-MgO sample. This technique enables the accurate mapping of B and Mg on the mixed oxide, with high resolution. The image in Figure 7b-ii was deconvoluted into the contributions from the B-K ionization edge ($\approx 193 \text{ eV}$) and Mg-L₂/L₃ ionization edge ($\approx 51 \text{ eV}$), which allowed us to obtain the detailed quantification of B

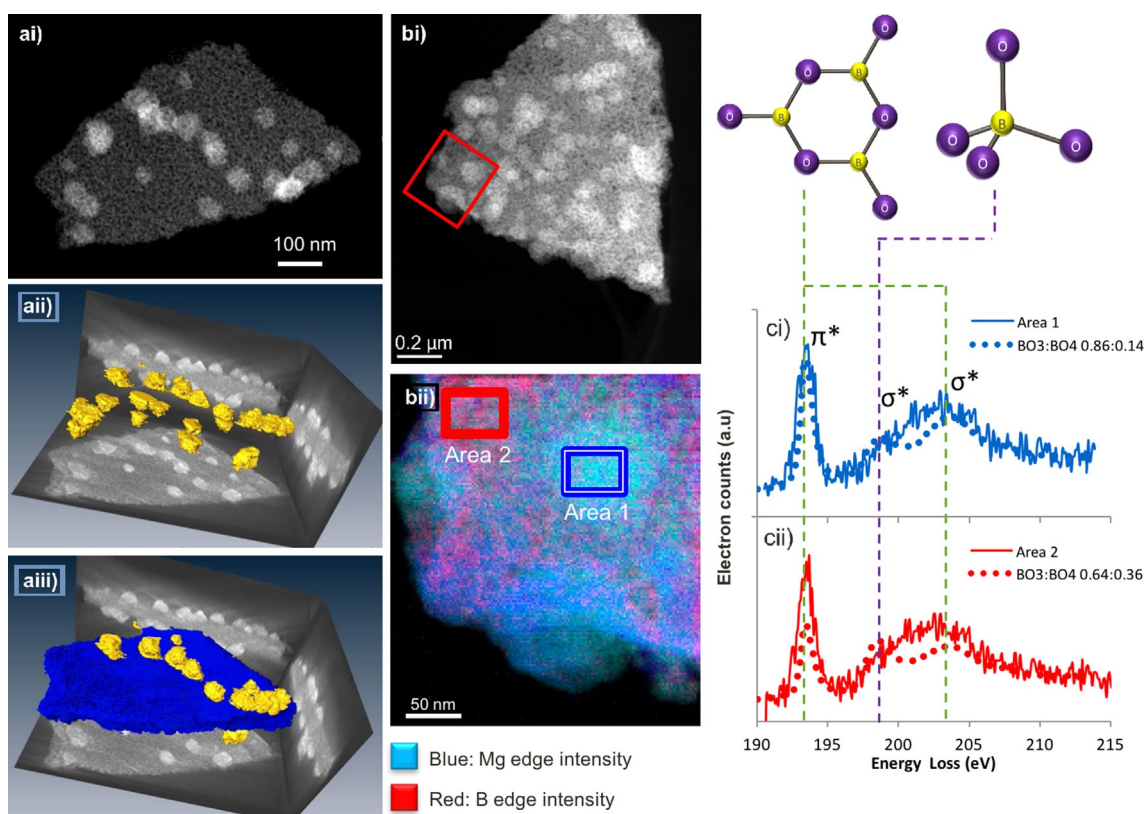


Figure 7. B mapping and electronic coordination on the B–MgO catalyst with 7.5 wt.% B prepared by combustion method. ai–aiii) Spatial HAADF–STEM tomography. b) AC–STEM analysis. bii) EELS mapping of Mg (blue) and B (red). ci,cii) B K-edge spectra of Area 1 and Area 2 in (bii), respectively. The spectra are offset from each other vertically for clarity. Dotted lines represent the fitting of a linear combination of reference BO_3 and BO_4 EELS spectra obtained for Area 1 and 2 (see text).^[34] Dashed vertical lines mark the characteristic peaks at 193 eV and 204 eV assigned to π^* and σ^* transitions of BO_3 (green) and 198 eV to σ^* states in BO_4 (purple).

(red) and Mg (blue) at nanometric resolution, with a scanning pixel of 2×2 nm. Notably, the clusters of 80–100 nm located on the surface of the mixed oxide are composed primarily of Mg with a small concentration of B. By contrast, the flat planes show a higher concentration of B. Therefore, it can be concluded that B-doped MgO possess two different types of surfaces with different chemistry and architecture. The B–K spectra showed fingerprints of different B coordination environments, that is, tetrahedral BO_4 and trigonal BO_3 (Figure 7cii). The catalyst and reference fingerprint spectra of BO_3 (trigonal) and BO_4 (tetrahedral) units were found in minerals vosenite ($[(\text{Fe}_{1-x}\text{Mg}_x)]_2\text{FeBO}_3$) and rhodizite ($\text{M}_{0.9}\text{Al}_4\text{B}_{11.35}\text{O}_{28}$), respectively.^[34] Area 1 was centered on one large surface cluster with low B concentration, and Area 2 was located on the flat surface with high B-concentration. In both regions, a large peak at 193 eV can be identified and a broad peak at 204 eV corresponding to trigonal B (BO_3).^[39,40] The first peak can be attributed to transitions to π^* molecular orbital (MO), whereas the broad peak at 204 eV is assigned to transitions to the σ^* MO.^[40] Detailed analysis of these spectra revealed that in Area 2 (Figure 7cii) the broad peak at 204 eV has a small shoulder at 198 eV. MO theory calculations have shown that in BO_4 a strong peak at 198.6 eV arises from transitions to σ^* final states. By fitting a linear combination of BO_3 and BO_4 reference spectra to the results shown in Figure 7ci,cii we could obtain

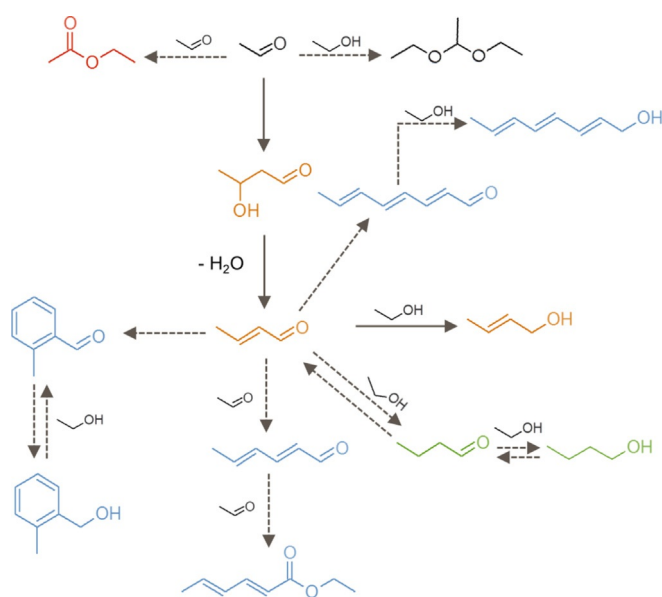
a semiquantitative estimate of the BO_3 : BO_4 ratio.^[41] The results shown in Figure 7ci,cii indicate that for Area 1 (flat surface) the ratio of BO_3 to BO_4 is 0.86:0.14, and for Area 2 (large clusters) this ratio decreases to 0.64:0.36. Importantly, these are semiconductive samples and BO_4 could undergo a transition to BO_3 under beam exposure. Therefore, care must be taken to avoid overexposure of the sample to the electron beam.^[42] These results show that BO_3 and BO_4 exist in both regions, but in different proportions. The fact that only a fraction of B is interstitial and the small crystalline radius of trigonal B and tetrahedral B^{3+} (0.15 Å and 0.25, respectively), compared to that of octahedral Mg^{2+} (1.03 Å), explain the small increment in lattice constant observed by XRD analysis.^[43]

As shown by ^{11}B NMR spectroscopy of 7.5 wt.% B–MgO, the fractions of interstitial BO_3 and $\text{BO}_{3/2}$ polymer are approximately 0.61 and 0.21, and that of interstitial BO_4 is 0.18, which results in a ratio BO_3 : BO_4 of 0.82:0.18 (see Figure 5). This value is very similar to the one obtained for Area 1 (0.86:0.14), indicating that on these large clusters with low B concentrations the majority of B is trigonal (BO_3) and interstitial. In contrast, the regions where B content was high, such as Area 2, interstitial B can occupy high-energy coordination positions such as BO_4 , whereas the rest of B forms a glassy B_2O_3 polymeric matrix on top of B–MgO. This explains the slow increase in acidity observed by pyridine TPD with the concentration of B. That is, at

low B concentrations, the majority of the B is interstitial and therefore the acidity does not increase until an excess of B exists on the surface to form glassy B_2O_3 . In sharp contrast, the basicity decreases significantly with even small concentrations of B, an indication of the strong passivation effect that interstitial B may have on MgO.

Synthesis of α - β unsaturated alcohols and aldehydes

Production of high-value chemicals from ethanol by aldol condensation requires fine-tuning of the chemical and structural properties of the catalyst to avoid undesired overcondensation and acetalization reactions. For this purpose, the catalysts in the B–MgO series with B concentrations ranging from 2.5 to 15.0 wt.% were tested in the conversion of ethanol and acetaldehyde to α - β unsaturated alcohols and aldehydes. As shown in Table S8, the main products from this reaction were crotonaldehyde (CAL) and crotyl alcohol (COH), which resulted from the dimerization of acetaldehyde through aldol condensation followed by Meerwein–Ponndorf–Verley (MPV) reduction, which converts crotonaldehyde into crotyl alcohol, with ethanol acting as the H donor. This main pathway competes with the formation of different side products, which include ethyl acetate, ethyl hexenoate and 2,4-hexadienal (mixed C6), 2,4,6-octatrienal and tolualdehyde (mixed C8). These products result from coupling and rearrangement reactions, such as Tishchenko reaction, aldol condensation, Michael addition, and ring closing/dehydrogenation reaction (Scheme 1). Small amounts of butyraldehyde (BAL) were also observed, as a result of H transfer to C=C double bond in crotonaldehyde. In addition, further MPV reduction of C=O of butyraldehyde and C=C of crotyl alcohol yields 1-butanol (BOH). Ethanol and acetaldehyde undergo acetalization to yield 1,1-diethoxyethane. Other products, including diethyl ether and 3-hydroxybutanal were



Scheme 1. Reaction network observed during ethanol and acetaldehyde condensation on MgO catalyst doped with boron.

also detected, but in trace amounts. Notably, the yield towards mixed C6 and C8 sharply decreased from 44 to 3.86 mol% as the concentration of B increased from 0 to 15 wt.% (Figure 8a). In contrast, crotonaldehyde (CAL), crotyl alcohol (COH), and 3-buten-1-ol (3BOH) significantly increased with B content, reaching a maximum yield of 72 mol% at a loading of 7.5 wt.% B–MgO. Butanol and butanal (BAL+BOH) followed the same trend, increasing from 2.16 to 10.4 mol% for B contents varied from 0 to 7.5 wt.%. However, further increase in B loading had a negative effect on the yield of CAL+COH+3BOH and BAL+BOH.

The selectivity of the MPV reaction to either C=O or C=C hydrogenation is controlled by the catalyst electronegativity, that is, acid–base character.^[44,45] This explains the increasing BAL and BOH formation as the B content increased. Further increment in B content beyond 7.5 wt.% was detrimental for CAL production and, in consequence, BAL and BOH formation. In turn, the acid-catalyzed acetalization was favored as the concentration of B exceeded 7.5 wt.%. As shown in Figure 8b the surface rate of reaction progressively increased with B loading from 0.16 to 2.82 molm⁻²h⁻¹ for 0 and 15 wt.% of B, respec-

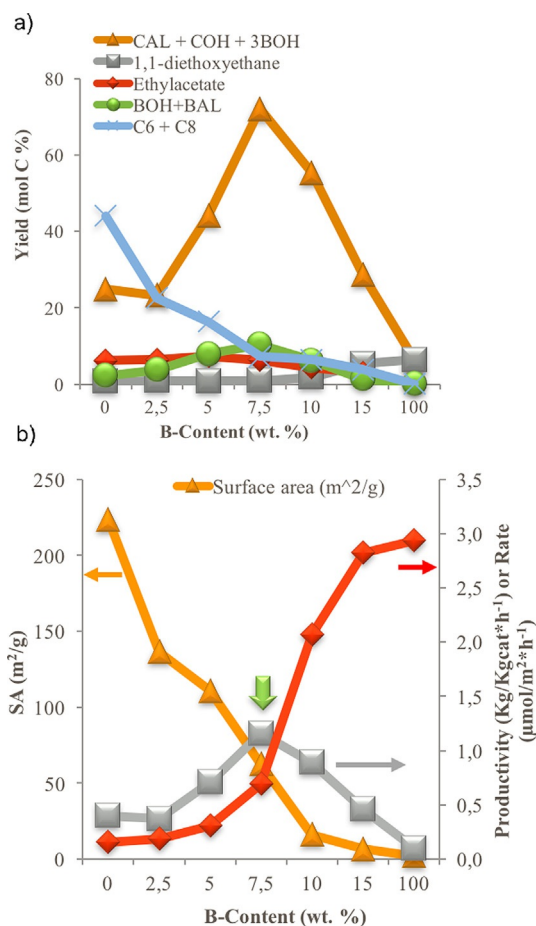


Figure 8. Relationship between structure–chemistry–activity on B–MgO. a) Product yields obtained as a function of B loading. b) Surface area (orange), reaction rate (red), and productivity (gray) toward COH and CAL + COH + 3BOH obtained as a function of B content for the aldol condensation of ethanol (20 mL) and acetaldehyde (2 mL) at 250 °C, 400 rpm, and 300 psi (20.7 bar) N₂ after 4 h reaction time in the presence of catalyst (200 mg).

tively. This enhanced reaction rate can be attributed to the stronger stabilization of chemisorbed carbonyl on surface B^{3+} cations compared to that on Mg^{2+} . Boric acid and boron oxide are reported as highly efficient catalysts for selective aldol condensation of aldehydes in hexane. In the presence of small concentrations of water, however, B_2O_3 is hydrated forming strong acidic Brønsted acid sites that favored over-condensation reactions.^[46] For B–MgO catalysts prepared by combustion, B cations are located in different chemical environments depending on the concentration as revealed by ^{11}B NMR spectroscopy. At low concentrations, the majority of B atoms are highly dispersed on the MgO forming a B_2O_3 –MgO interface. In highly refractory oxides, such as MgO, the surface energy is dramatically reduced if low-melting-point oxides such as B_2O_3 are added.^[47] Thereby, it is likely that B cations migrate to these high-energy sites during the combustion process (e.g., MgO defects) to lower the surface Gibbs free energy, and only a small fraction of B^{3+} is stabilized in the MgO lattice. Once the concentration is sufficiently high, that is, >7.5 wt. % B, the surface and lattice of MgO is significantly enriched with B and finally the small nucleation sites of glassy B_2O_3 become sufficiently large to form pure B_2O_3 with its characteristic acid character. This has a two-fold effect. First, the highly dispersed glassy B_2O_3 neutralizes the strongest basic sites by forming a passivating layer on MgO, which reduces the basicity and significantly increases acidity once the concentration is above 7.5 wt. % B–MgO. This accelerates the rate of acid-catalyzed condensation on hydrated B_2O_3 –MgO.

Second, interstitial B passivates the growth of highly basic facets, such as (111) surface, making the surface oxygen electron deficient (as shown by X-ray photoelectron spectroscopy in Figure S1). Notably, this enhancement in surface activity was accompanied by a marked decrease in specific surface area (i.e., from 223.5 in pure MgO to $6.7\text{ m}^2\text{ g}^{-1}$ in 15 wt. % B–MgO). In turn, the productivity of CAL + COH + 3BOH was significantly lower. At intermediate B concentrations (e.g., 7.5 wt. % B–MgO) the CAL + COH + 3BOH yield reached a maximum, $1.16\text{ kg}_{\text{product}}\text{ kg}_{\text{catalyst}}^{-1}\text{ h}^{-1}$, compared to the 0.4 and $0.1\text{ kg}_{\text{product}}\text{ kg}_{\text{catalyst}}^{-1}\text{ h}^{-1}$ observed on pure MgO and pure B_2O_3 , respectively. In addition, the TPD results for CO_2 reveal that upon addition of boron the surface basicity decreases dramatically (see Table S3) from $419.27\text{ }\mu\text{mol g}^{-1}$ (pure MgO) to 0 (pure B_2O_3). The results clearly show that in the absence of boron the concentration of high-strength basic sites, identified by the formation of unidentate carbonate CO_2 on the surface, dominates over those associated with the bidentate carbonate and bicarbonate. Upon addition of boron, this profile changed drastically. At 7.5 wt. % B–MgO the total concentration of basic sites decreased and, more importantly, the basic sites with high strength disappeared. As a result, the remaining basic sites are located in the range of medium temperature desorption, corresponding to bidentate carbonate. This reduction in basicity of the catalyst explains the reduction in the formation of heavy condensation products (C6 + C8), and the production of C4 products remains high. The reduction in basicity is accompanied by an increase in acidity as the concentration of boron increases (see Figure S3). The TPD results for pyridine

reveal that with 7.5 wt. % B–MgO the total concentration of acid sites is significantly higher than that observed on 2.5 wt. % B–MgO. More importantly, the fraction of strong acid sites increases considerably. This enhancement in total concentration and strength of the acid sites in the catalyst is critical for the dehydration of the 3-hydroxybutanal and selective reduction of the C4 aldehyde to the C4 alcohols by the MPV reaction.

The stability and deactivation of the catalyst is an important aspect that needs to be addressed. Experiments were performed with the fresh 7.5 wt. % B–MgO sample (first cycle test) and the recycled ones (second cycle test and thereafter). As shown in Table S11, the total product and CAL + COH + 3BOH product yields decreased for the second and third cycle tests, but the fourth cycle test gave similar yields to the third cycle. These results indicate that catalyst leaching and blockage of some active sites may occur from the production of large hydrocarbon molecules at the beginning of the reaction, but they also suggest that significant stability is reached after a couple of reaction cycles. More importantly, the original catalytic activity can be fully recovered by regeneration at 500°C .

Conclusions

B-doped MgO catalysts with tailored properties were synthesized by a combustion method that employs citric acid as a fuel. The large melting point differences between B_2O_3 and MgO make it possible to form a metastable structure of B-doped MgO with hierarchical porous structure consisting of an interconnected network of mesopores and macrochambers, which facilitate molecular diffusion out of the catalyst. This technique requires the utilization of oxides with significantly different melting points to obtain the hierarchical porous structure and the proper selection of the valence and loading of the low-melting-point metal oxide to avoid significant losses in surface area. In this case, the 7.5 wt. % B on MgO was the optimal composition that resulted in the highest yield towards the desired products by the proper balance of acid–base properties, meso-/macroporosity, and surface area. The material showed minimal loss in catalytic activity after four cycles of reaction. Moreover, the catalyst performance was fully regained after regeneration at 500°C . We envision that this catalyst preparation technique can be applied to other catalytic systems to obtain highly accessible materials with nanocontrolled architecture and surface chemistry for diverse applications in commodity chemicals production, conversion of bioderived feedstocks, CO_2 capture, environmental remediation, and energy storage.

Experimental Section

Catalyst preparation

Pure MgO and B_2O_3 were purchased from Alfa Aesar and used without further modification. B-doped MgO samples were prepared by the thermal decomposition (citrate–nitrate combustion) method,^[48] using $Mg(NO_3)_2$ (Sigma–Aldrich, 99%) and B_2O_3 (Alfa Aesar, 99.99%) as precursors. Different ratios of $Mg(NO_3)_2$ and B_2O_3

corresponding to different final compositions were dissolved in de-ionized water. As soon as the solution became clear, citric acid was added in a proportion of 1.2 moles of the acid per mole of metal atom. The mixture was then heated on a hot plate (at 140 °C) for 1 h to evaporate the water. After that, it was quickly transferred and combusted inside an oven preheated to 550 °C. The ashes obtained after combustion were calcined at 550 °C for 12 h in air to eliminate the carbonaceous residues. The resulting material was then ground into a fine powder for use and labeled xB–MgO with x as the weight percentage loading of Boron. For comparison purpose, a 2 wt.% loading of B on MgO catalyst was prepared by conventional incipient wetness impregnation of an aqueous solution of B₂O₃ (Alfa Aesar, 99.999%) onto MgO support (Alfa Aesar, 96%), at a liquid/solid ratio of 0.15 mLg⁻¹. After impregnation, the catalyst was dried overnight in an oven at 400 °C.

Characterization methods

The BET surface area of the catalyst was measured by N₂ physisorption at liquid nitrogen temperature on a Micromeritics ASAP 2010 unit. For these measurements, the sample was degassed for 12 h at 250 °C prior to the analysis. XRD analysis was conducted on a Rigaku automatic diffractometer (Model D-MAX A), equipped with a curved crystal monochromator and system setting of 40 kV and 35 mA. Data were collected over 5–40° angle range with a step size of 0.05 and a count time of 1.0 s. The basic properties of the catalysts were characterized by using TPD of CO₂. A 100 mg sample was heated in the TPD system under a He flow of 30 mL min⁻¹ to 200 °C with a heating rate of 10 °C min⁻¹ and held at this temperature for 3 h. The sample was then cooled down to RT and pure CO₂ at a flow rate of 30 mL min⁻¹ was then passed through the sample for 30 min. The sample was subsequently purged with He for 2 h to remove the physisorbed CO₂. TPD was performed under the same He flow rate by heating from 0 to 600 °C with a heating rate of 10 °C min⁻¹. XPS analysis of catalysts was performed using a PHI 5800 ESCA (Physical Electronics) system equipped with a standard achromatic Al_{Kα} X-ray source (1486.6 eV) operating at 300 W (15 kV and 20 mA) and a concentric hemispherical analyzer. The PHI Model 04–110 vacuum transfer vessel was used to hold and transfer the ex situ dehydrated samples from a glove bag to the analysis chamber without atmospheric exposure. The catalyst powder samples were dusted on to double-sided conductive carbon tape mounted on XPS sample holder. Survey spectra (0–1400 eV) and high-resolution spectra were collected with a pass energy of 187.85 eV and 23.50 eV respectively. All data were collected at 45° takeoff angle. To compensate for surface charging effects, all spectra were referenced to the hydrocarbon C 1s peak at 284.6 eV. ¹¹B NMR experiments were performed on a Bruker AVIII HD NMR spectrometer operating at a magnetic field strength of 11.74 T with a 4 mm Bruker MAS probe. For the MAS experiments of ¹¹B (160.5299 MHz), a single pulse acquisition was applied with a spinning speed of 14 KHz and a short RF pulse (less than 15°) with a recycle delay of 15–20 s. Spectra were collected after 4096 scans and referenced to solid NaBH₄ at –42.16 ppm. SEM imaging was performed on a Zeiss NEON 40 EsB system equipped with a Schottky emitter electron source, and operated at an accelerating voltage of 2 kV using secondary electrons as the major signal source. HAADF–STEM and HRTEM characterization were performed by using a FEI Tecnai F30, operated at 300 kV equipped with a Gatan CCD camera, an EDS (EDAX) detector, and a Gatan Tridiem Energy Filter. AC–STEM analyses were performed in a XFEI FEI Titan 60–300, operated at 300 kV, equipped with a monochromator, EDX detector and a Gatan Tridiem Energy Filter.

The microscope possesses a CEOS spherical aberration corrector for the electron probe allowing a resolution of 0.8 Å.

Catalytic reaction experiments

The liquid-phase catalytic MPV reaction of acetaldehyde (99%, Sigma Aldrich) and ethanol (100%, Pharmco AAPER) was studied in a 50 mL stainless-steel autoclave batch reactor (Parr Corporation), equipped with an impeller, temperature, and pressure controllers. In a typical experiment, measured amounts of catalyst were mixed with 20 mL ethanol and 2 mL acetaldehyde and placed in the reactor vessel. After the reactor was sealed, it was purged and pressurized with N₂ to 300 psi (20.7 bar) and heated up to 250 °C. High speed mechanical stirring kept the catalyst suspended to avoid external mass transfer limitations. After the reaction, products were filtered and analyzed using gas chromatography (GC). Product identification was done on GC–MS (Shimadzu QP2010S) equipped with a ZB-1701 column, 60.0 m × 0.25 μm nominal. GC–FID (Agilent 7890B) with a capillary column of poly(ethylene glycol) (ZB-WAX) of 60.0 m × 0.25 mm × 0.25 μm nominal was employed for quantification, using the corresponding chemical standards to obtain response factors. All the yields were calculated in carbon molar base. The detectable products consisted of crotonaldehyde, crotyl alcohol, 3-buten-1-ol, butanal, butanol, 1,1-diethoxyethane, ethyl acetate, mixed C6 (2,4-hexadienal), and mixed C8 (2,4,6-octatrienal, *meta*- or *ortho*-tolualdehyde, ethyl-3-hexenoate, and ethylhexanoate).

Acknowledgements

The authors acknowledge the financial support provided by the Centro para el Desarrollo Tecnológico Industrial (CDTI) and the Agencia IDEA. We also would like to thank Drs. S. P. Crossley, T. Sooknoi, and R. E. Jentoft for valuable discussions and technical assistance on metal oxides characterization and C–C coupling reactions. The Institute of Nanoscience of Aragón (INA) is acknowledged for their guidance and assistance in the acquisition of the AC–TEM–EELS and FIB–SEM–EDS analyses and 3D reconstruction.

Keywords: aldol reaction • boron • doping • magnesium • mesoporous materials

- [1] M. A. Aramendía, V. Boráu, C. Jiménez, J. M. Marinas, A. Porras, F. J. Urbano, *J. Mater. Chem.* **1999**, *9*, 819–825.
- [2] H. Hattori, *Chem. Rev.* **1995**, *95*, 537–558.
- [3] A. M. Youssef, L. B. Khalil, B. S. Girgis, *Appl. Catal. A* **1992**, *81*, 1–13.
- [4] J. Sun, K. Zhu, F. Gao, C. Wang, J. Liu, C. H. F. Peden, Y. Wang, *J. Am. Chem. Soc.* **2011**, *133*, 11096–11099.
- [5] E. Dumitriu, V. Hulea, C. Chelaru, C. Catrinescu, D. Tichit, R. Durand, *Appl. Catal. A* **1999**, *178*, 145–157.
- [6] H. Tsuji, F. Yagi, H. Hattori, H. Kita, *J. Catal.* **1994**, *148*, 759–770.
- [7] L. Faba, E. Díaz, S. Ordóñez, *Appl. Catal. B* **2012**, *113–114*, 201–211.
- [8] L. Faba, E. Díaz, S. Ordóñez, *ChemSusChem* **2013**, *6*, 463–473.
- [9] P. Kuśtrowski, D. Sulkowska, L. Chmielarz, A. Rafalska-Lasocha, B. Dudek, R. Dziembaj, *Microporous Mesoporous Mater.* **2005**, *78*, 11–22.
- [10] J. Wallot, P. Reynders, J. Rödel, *J. Am. Ceram. Soc.* **2008**, *91*, 3856–3863.
- [11] Q. Zeng, W. Li, J. Shi, J. Guo, H. Chen, M. Liu, *J. Eur. Ceram. Soc.* **2007**, *27*, 261–265.
- [12] D. W. Kim, K. S. Hong, C. S. Yoon, C. K. Kim, *J. Eur. Ceram. Soc.* **2003**, *23*, 2597–2601.

- [13] W. Janssens, E. V. Makshina, P. Vanelderen, F. De Clippel, K. Houthoofd, S. Kerkhofs, J. A. Martens, P. A. Jacobs, B. F. Sels, *ChemSusChem* **2015**, *8*, 994–1008.
- [14] A. Corma, S. Iborra, A. Velty, *Chem. Rev.* **2007**, *107*, 2411–2502.
- [15] J. Scalbert, F. Thibault-Starzyk, R. Jacquot, D. Morvan, F. Meunier, *J. Catal.* **2014**, *311*, 28–32.
- [16] C. Angelici, B. M. Weckhuysen, P. C. A. Bruijninx, *ChemSusChem* **2013**, *6*, 1595–1614.
- [17] Y. Tanaka, Y. Imizu, H. Hattori, K. Tanabe, *Stud. Surf. Sci. Catal.* **1981**, *7*, 1254–1267.
- [18] A. Gervasini, *J. Catal.* **1991**, *131*, 190–198.
- [19] R. Sokoll, H. Hobert, *J. Catal.* **1992**, *134*, 409–421.
- [20] D. J. Pine, A. Imhof, *Nature* **1997**, *389*, 948–951.
- [21] S. Gheorghiu, M. O. Coppens, *AIChE J.* **2004**, *50*, 812–820.
- [22] R. M. Hazen, *Am. Mineral.* **1976**, *61*, 266–271.
- [23] O. M. Moon, B. C. Kang, S. B. Lee, J. H. Boo, *Thin Solid Films* **2004**, *464–465*, 164–169.
- [24] X. Liu, S. Ye, Y. Qiao, G. Dong, Q. Zhang, J. Qiu, *Chem. Commun.* **2009**, 4073–4075.
- [25] P. W. Tasker, *J. Phys. C* **1979**, *12*, 4977–4984.
- [26] J. G. Fripiat, A. A. Lucas, J. M. André, A. G. Derouane, *Chem. Phys.* **1977**, *21*, 101–104.
- [27] a) A. Wander, I. J. Bush, N. M. Harrison, *Phys. Rev. B* **2003**, *68*, 233405.
- [28] E. G. Derouane, V. Jullien-Lardot, R. J. Davis, N. Blom, P. E. Hojlund-Nielsen, *Stud. Surf. Sci. Catal.* **1993**, *75*, 1031–1042.
- [29] P. E. Hojlund-Nielsen, *Nature* **1977**, *267*, 822.
- [30] M. Kiguchi, S. Entani, K. Saiki, T. Goto, A. Koma, *Phys. Rev. B* **2003**, *68*, 115402.
- [31] J. Yoon, K. Kim, *Appl. Phys. Lett.* **1995**, *66*, 2661.
- [32] K. P. Peil, L. G. Galya, G. Marcelin, *J. Catal.* **1989**, *115*, 441–451.
- [33] N. Feng, A. Zheng, Q. Wang, P. Ren, X. Gao, S. B. Liu, Z. Shen, T. Chen, F. Deng, *J. Phys. Chem. C* **2011**, *115*, 2709–2719.
- [34] J. A. Rodriguez, R. A. Campbell, D. W. Goodman, *J. Phys. Chem.* **1991**, *95*, 5716–5719.
- [35] J. S. Corneille, J.-W. He, D. W. Goodman, *Surf. Sci.* **1994**, *306*, 269–278.
- [36] J. Chen, S. Tian, J. Lu, Y. Xiong, *Appl. Catal. A* **2015**, *506*, 118–125.
- [37] K. Zhu, J. Hu, C. Kübel, R. Richards, *Angew. Chem. Int. Ed.* **2006**, *45*, 7277–7281; *Angew. Chem.* **2006**, *118*, 7435–7439.
- [38] S. Auzary, F. Pailloux, M. F. Denanot, R. J. Gaboriaud, *Thin Solid Films* **1998**, *319*, 163–167.
- [39] R. Brydson, D. D. Vvedensky, W. Engel, H. Sauer, B. G. Williams, E. Zeitler, J. M. Thomas, *J. Phys. Chem.* **1988**, *92*, 962–966.
- [40] H. Sauer, R. Brydson, P. N. Rowley, W. Engel, J. M. Thomas, *Ultramicroscopy* **1993**, *49*, 198–209.
- [41] S. Cheng, G. Yang, Y. Zhao, M. Peng, J. Skibsted, Y. Yue, *Sci. Rep.* **2015**, *5*, 17526.
- [42] A. Manara, M. Antonini, P. Camagni, P. N. Gibson, *Nucl. Instrum. Methods Phys. Res. Sect. B* **1984**, *1*, 475–480.
- [43] R. D. Shannon, *Acta Crystallogr. Sect. A* **1976**, *32*, 751–767.
- [44] J. J. Ramos, V. K. Diez, C. A. Ferretti, P. A. Torresi, C. R. Apesteguía, J. I. Di Cosimo, *Catal. Today* **2011**, *172*, 41–47.
- [45] F. Braun, J. I. Di Cosimo, *Catal. Today* **2006**, *116*, 206–215.
- [46] R. D. Offenhauer, S. F. Nelsen, *J. Org. Chem.* **1968**, *33*, 775–777.
- [47] *Fiberglass and Glass Technology Energy-Friendly Compositions and Applications* (Eds.: F. T. Wallenberger, P. A. Bingham), Springer Science+Business Media, New York. **2010**.
- [48] E. Flahaut, C. Laurent, A. Peigney, *Carbon* **2005**, *43*, 375–383.

Received: August 3, 2016

Published online on October 31, 2016